Hindawi
Journal of Nanomaterials
Volume 2019, Article ID 1703218, 9 pages
https://doi.org/10.1155/2019/1703218

Research Article

Transition Metal Oxides on Reduced Graphene Oxide Nanocomposites: Evaluation of Physicochemical Properties

Vincenza Modafferi,[1] Saveria Santangelo,[1] Michele Fiore,[2] Enza Fazio,[3] Claudia Triolo,[3] Salvatore Patanè,[3] Riccardo Ruffo,[2] and Maria G. Musolino[1]

[1]*Università "Mediterranea", Dipartimento di Ingegneria Civile, dell'Energia, dell'Ambiente e dei Materiali (DICEAM), Via Graziella, Loc. Feo di Vito, 89122 Reggio Calabria, Italy*
[2]*Dipartimento di Scienza dei Materiali, Università degli Studi di Milano Bicocca, 20125 Milano, Italy*
[3]*Università di Messina, Dipartimento di Scienze Matematiche e Informatiche, Scienze Fisiche e Scienze della Terra (MIFT), Viale Stagno d'Alcontres 31, 98166 Messina, Italy*

Correspondence should be addressed to Salvatore Patanè; salvatore.patane@unime.it

Received 30 September 2018; Accepted 10 December 2018; Published 11 April 2019

Academic Editor: Xuping Sun

Transition metal oxides on reduced graphene oxide (TMO@rGO) nanocomposites were successfully prepared via a very simple one-step solvothermal process, involving the simultaneous (thermal) reduction of graphene oxide to graphene and the deposition of TMO nanoparticles over its surface. Texture and morphology, microstructure, and chemical and surface compositions of the nanocomposites were investigated via scanning electron microscopy, X-ray diffraction, micro-Raman spectroscopy, and X-ray photoelectron spectroscopy, respectively. The results prove that Fe_2O_3@rGO, $CoFe_2O_4$@rGO, and CoO@rGO are obtained by using Fe and/or Co acetates as oxide precursors, with the TMO nanoparticles uniformly anchored onto the surface of graphene sheets. The electrochemical performance of the most promising nanocomposite was evaluated as anode material for sodium ion batteries. The preliminary results of galvanostatic cycling prove that Fe_2O_3@rGO nanocomposite exhibits better rate capability and stability than both bare Fe_2O_3 and Fe_2O_3+rGO physical mixture.

1. Introduction

Recently, graphene-based nanocomposites have captured considerable attention due to their unique properties and the large variety of possible applications, ranging from sensing and energy storage to heterogeneous, electro-, and photocatalysis [1–6]. Thanks to the striking combination of high specific surface area [7], chemical inertness [8], great mechanical strength [9], and excellent electrical and thermal conductivities [10], the utilization of graphene as an active support framework for functional nanoparticles (NPs) has open promising research areas. Various methods have been developed for the synthesis of graphene, through either chemical or physical routes [3, 11–14]. Among them, chemical oxidation of graphite to graphene oxide (GO), followed by reduction to produce graphene nanosheets, results to be the most appealing due to its low cost, ease, and high yield [8, 15]. GO possesses a considerable fraction of sp^3-hybridized carbon atoms, covalently decorated with oxygen-containing functional groups. These oxygen-containing functional groups, including hydroxyl and epoxy groups mainly at basal planes of the carbon sheets and carbonyl and carboxylic groups prevailingly at the edges, provide GO with a remarkable hydrophilic character and chemical reactivity. Furthermore, the oxygen-containing functionalities can act as potential anchoring sites for adsorbing diverse metal oxide NPs [4, 7, 16].

Graphite powders represent nowadays the standard anode material for commercial secondary Li^+ ion batteries. Recently, many metal oxides have been evaluated as alternative anode materials both in Li^+ and Na^+ ion batteries (LIBs and SIBs) [17–19]. Among transition metal oxides (TMOs),

which store Li^+ or Na^+ ions via conversion reactions [20], hematite (α-Fe_2O_3), magnetite (Fe_3O_4), and spinel cobalt oxide (Co_3O_4) are attracting great attention, thanks to their high theoretical specific capacities (1007 mAh/g, 926 mAh/g, and 890 mAh/g, respectively) [21–24]. Unfortunately, most of the TMO anodes suffer from limited cycle life as an effect of the large volume changes occurring during the conversion reactions. It is well accepted that graphene is able to buffer the volume expansion/contraction of TMOs in the composites during electrochemical reactions [25–28], thus limiting their pulverisation. Indeed, the iron oxide-rGO composites synthesized via microwave-assisted methods by Zhang et al. [29] taking advantage of the small particle size and the beneficial properties of rGO can deliver up to 300 mAh/g for more than 140 cycles. The specific capacity of ordered nitrogen-doped carbon/γ-Fe_2O_3 synthesized by Qiang et al. [30] through a multistep approach exceeded 200 mA/g at 100 mA/g (C/10), whereas the iron oxide-rGO composite prepared by the microwave-assisted method by Liu et al. [31] delivered 289 mAh/g at 100 mA/g, remaining stable for 50 cycles.

In this work, we report the synthesis of nanostructured composites, consisting of cobalt and/or iron oxide anchored on GO, by the one-step solvothermal approach. The main advantage of this method is that since the reduction of GO to rGO occurs simultaneously to the deposition of the TMO NPs, it does not require the use of any chemical-reducing agent. Textural, structural, and morphological properties of the nanocomposites are studied by several complementary analysis techniques in view of their possible application as electrode materials in rechargeable batteries. Preliminary results relative to the electrochemical performance of the most promising of them are presented revealing that the carbon oxide nanocomposite shows good electrochemical performance in terms of specific capacity and capacity retention.

2. Materials and Methods

2.1. Materials. Sodium nitrate ($NaNO_3$, 99.5% purity), sulfuric acid (H_2SO_4, 95-97% purity), and propylene carbonate (anhydrous, purity ≥ 99.9%) were purchased from Merck. Potassium permanganate ($KMnO_4$, ACS reagent purity ≥ 99.0%), graphite powder (purum, particle size ≤ 0.1 mm), iron (II) acetate ($Fe(CH_3COO)_2$, 95% purity), cobalt (II) acetate tetrahydrate ($Co(CH_3COO)_2{\cdot}4H_2O$, 99.999% purity), N-methyl-2-pyrrolidone (ACS reagent, 99% purity), sodium perchlorate ($NaClO_4$, ACS reagent, purity ≥ 98%), and fluoroethylene carbonate (99.9% purity) were supplied from Sigma-Aldrich. Hydrochloric acid (HCl, 36% wt) was obtained from Alfa Aesar. Hydrogen peroxide (H_2O_2, 30% wt) and ethanol 96° were purchased from Carlo Erba Reagents. All the chemicals were used as received without further purification. Distilled water was used throughout the experiments.

2.2. Synthesis of Graphene Oxide. Graphene oxide was prepared by exfoliation of graphite powder following a slightly modified Hummers method [32]. In a typical synthesis, 2 g of graphite and 1 g of $NaNO_3$ were mixed with 50 ml of concentrated H_2SO_4 and stirred in an ice bath. Subsequently, $KMnO_4$ (7 g) was slowly added into the mixture under stirring and cooling. The mixture was stirred for 2 h at 35°C. The temperature was then increased to about 98°C, and distilled water (400 ml) was added followed by a slow addition of 10 ml of H_2O_2 under stirring. The colour of the suspension turned from brown to yellow. The as-obtained GO was then recovered through centrifugation and thoroughly washed with HCl aqueous solution and with distilled water, in sequence. Finally, the solid was dried at 50°C in a vacuum oven for 2 days. Upon the solvothermal treatment, at 170°C for 3 h (see below), GO thermally reduced to rGO.

2.3. Synthesis of TMO/rGO Nanocomposite. The nanocomposites were obtained by the solvothermal treatment sketched in Figure S1. 200 mg of GO was dispersed in 60 ml of ethanol through sonication for 2 h. Then, 10 ml of a 0.2 M solution of $Fe(CH_3COO)_2$ or of $Co(CH_3COO)_2{\cdot}4H_2O$ was added. The reaction mixture was stirred at 80°C for 10 h and, subsequently, was transferred in a Teflon beaker and sealed in a stainless steel autoclave for the solvothermal treatment at 170°C for 3 h. The resulting product was centrifuged, washed with ethanol and distilled water for several times, and then dried in air. A nanocomposite based on mixed metal oxides on GO was also prepared (the molar ratio of the Fe/Co precursors was 1 : 1). For comparison purposes, Fe_2O_3 NPs were also synthesized by the same procedure except for the absence of GO.

2.4. Material Characterization. The sample texture and morphology were investigated by scanning electron microscopy (SEM). Analysis was performed using a Phenom ProX scanning electron microscope equipped with an energy-dispersive X-ray (EDX) spectrometer.

The formation of GO and its subsequent reduction to rGO upon thermal treatment were ascertained by means of X-ray powder diffraction (XRD) and micro-Raman spectroscopy (MRS). The XRD patterns were recorded at RT by using the Ni β-filtered Cu-Kα radiation (λ = 0.15404 nm) at 40 kV. Analyses were registered in the 2θ range of 10–80° at a scan speed of 0.5°/min. Diffraction peak identification was performed on the basis of the JCPDS database of reference compounds. MRS analysis was carried out in air at room temperature. Raman scattering from the samples excited by an Nd:YAG laser operating at 532 nm (2.33 eV) aligned to a confocal microscope (NTEGRA-Spectra SPM from NT-MDT) and equipped with a 100x objective. A very low laser power (250 μW at the sample surface) was used in order to avoid local heating of the samples and annealing effects.

The crystalline phase of the oxide was identified via XRD and MRS analyses. Surface composition of the samples and chemical environment of the component species were investigated by X-ray photoelectron spectroscopy (XPS). Spectra were acquired using a K-Alpha system of Thermo Scientific, equipped with a monochromatic Al-Kα source (1486.6 eV) and operating in a constant analyzer energy (CAE) mode with a pass energy of 50 eV for high-resolution spectra and a spot size of 400 μm. The binding energy shifts were

calibrated keeping the C 1s position fixed at 284.5 eV. Identification and quantification of the surface species were carried out by decomposing the high-resolution photoelectron spectra of C 1s, O 1s, Fe 2p, and Co 2p core levels. The elemental concentrations were estimated from the areas under the photoelectron peaks weighed by the relative sensitivity factors. The results obtained are reported in Table S1.

2.5. Electrochemical Testing. Galvanostatic cycling with potential limitation (GCPL) was carried out with the Bio-Logic VSP-300 multichannel potentiostat/galvanostat on two-electrode coin cells CR2032 assembled in an argon-filled glove box (MBraun), with sodium acting both as counter and reference electrodes. The working electrode for galvanostatic cycling was prepared mixing Fe_2O_3@rGO composite, the carbon matrix (Super P, MM Carbon), and the polymer binder (polyacrylic acid Mw ~450,000, Sigma-Aldrich) in the weight ratio 8 : 1 : 1, respectively. A second electrode was made by using a physical mixture of Fe_2O_3 powder and rGO (Fe_2O_3+rGO) as an active material. For this purpose, Fe_2O_3 powder and rGO, synthesized separately, were mixed in the same ratio as Fe_2O_3@rGO nanocomposite. Finally, a third electrode was prepared by adding a higher carbon black content to bare Fe_2O_3 in order to obtain a comparable total carbon content with respect to the other electrodes. The conductive carbon matrix used in the preparation of the electrode was pretreated at 800°C under argon atmosphere, to remove the adsorbed water and impurities, reducing the typical irreversibility that occurs during the first charge and discharge in such systems [22]. The slurry obtained suspending the solid in N-methyl-2-pyrrolidone solvent was casted onto a copper foil using the doctor blade technique and subsequently dried at 80°C under vacuum overnight. The working electrode was then roll pressed, and 16 mm diameter disks were punched out. The load of active material was about 1 mg/cm^2. The electrolyte was a 1 M solution of $NaClO_4$ in anhydrous propylene carbonate with a 2% wt fluoroethylene carbonate additive. The GCPL tests were performed between 0.01 V and 3.00 V vs. Na/Na$^+$ at different C-rates.

3. Results and Discussion

3.1. Support. The formation of GO from graphite was ascertained by means of XRD (compare patterns a and b in Figure S2). The XRD pattern of GO shows the sharp and characteristic diffraction peak at $2\theta = 9.5°$, corresponding to the (001) reflection of graphene oxide with d-spacing of 0.955 nm. Its 2θ angle position, shifted to lower angles with respect to strong and sharp diffraction (002) of pristine graphite at 26.7°, matches well with the values reported in the literature [15], suggesting that GO sheets are loosely stacked due to the presence of oxygen-containing functional groups (C=O, –COOH, –OH, and C–O–C) between the layer of graphite formed during oxidation. The minor reflection at 42.6° suggests a turbostratic disorder in graphene sheets [33].

After the solvothermal treatment, the characteristic peak of GO disappears, confirming the occurrence of the thermal reduction to rGO. A very broad and intense peak around 2 $\theta = 24.1°$ and a weaker one around at $2\theta = 43.2°$ are detected (pattern c in Figure S2). The latter can be ascribed to the reflection from (100) plane of rGO. The former corresponds to the reflection from (002) plane with a d -spacing value of 0.369 nm. The remarkable decrease of interlayer spacing confirms the removal of most of the oxygen-containing functional groups [34].

The results of MRS and XPS analyses confirm the formation of rGO upon solvothermal reaction. The Raman spectra of GO and rGO (Figure S3) are dominated by two intense and broad bands at ~1360 cm^{-1} (D-band) and ~1590 cm^{-1} (G-band). The D-band is generated by finite size effects and by lattice defects breaking the translational symmetry of graphitic layers, while the G-band originates from the stretching of C=C pairs and is the fingerprint of the graphitic crystalline arrangement [35]. In the higher frequency region of the spectrum, overtones and combination bands are detected.

The D/G integrated intensity ratio (I_D/I_G) is commonly utilized to monitor the sp^2 defect density in the carbon lattice [36]. It enhances from 2.75 in GO to 3.01 in rGO, proving that the density of sp^2 carbon defects (the only ones contributing to the D-band intensity [35]) increases at expenses of non-sp^2 defects. In addition, the G-band, sensitive to charge transfer, local distortions, and hybridization changes of the C–C bonding [36], downshifts from 1600 cm^{-1} in GO to 1588 cm^{-1} in rGO owing to the oxidation degree lowering.

The high-resolution photoelectron profiles of the C 1s core levels in GO and rGO (Figure S4) are very different. In both the spectra, the contribution at 284.5 eV binding energy (BE) arises from C=C/C–C bonds in aromatic rings. Contributions ascribed to oxygenated carbon species fall in the 286–290 eV BE range. They include C–O species in phenols and ethers (at 286.1–286.3 eV), C=O species in carbonyls/quinones (at ~287.5 eV), and O–C=O bonds in carboxylic acid and anhydrides and esters (at 288.7 –289.3 eV) [36]. As evident, solvothermal treatment brings about a drastic decrease of the C–O and C=O species present on the carbon surface. In addition, the appearance in the HRXPS spectrum of rGO of a weak contribution at 290.5 –291.0 eV (shake-up π–π^* transition [36]), absent in the HRXPS spectrum of GO, indicates the partial restoration of the π network following the release of oxygenated functionalities upon thermal treatment. Finally, Figure S5 compares the morphology of GO support before and after solvothermal reaction. The GO sample shows highly porous agglomerates, while rGO exhibits a structure similar to crumpled and ripped flakes, confirming the reduction of GO.

3.2. Nanocomposites. Figure 1 displays the morphology of TMO@rGO nanocomposites, resulting from the SEM analysis. As particularly evident in the higher magnification images (Figures 1(d)–1(f)), the TMO NPs are uniformly confined in the wrinkled sheet-like structure of rGO, indicating that TMO NPs are successfully anchored on the graphene flakes during the solvothermal process. The average size of the oxide grains ranges between 45 and 70 nm.

Figure 2 shows XRD patterns of the investigated TMO@rGO nanocomposites. No typical diffraction peak of GO is

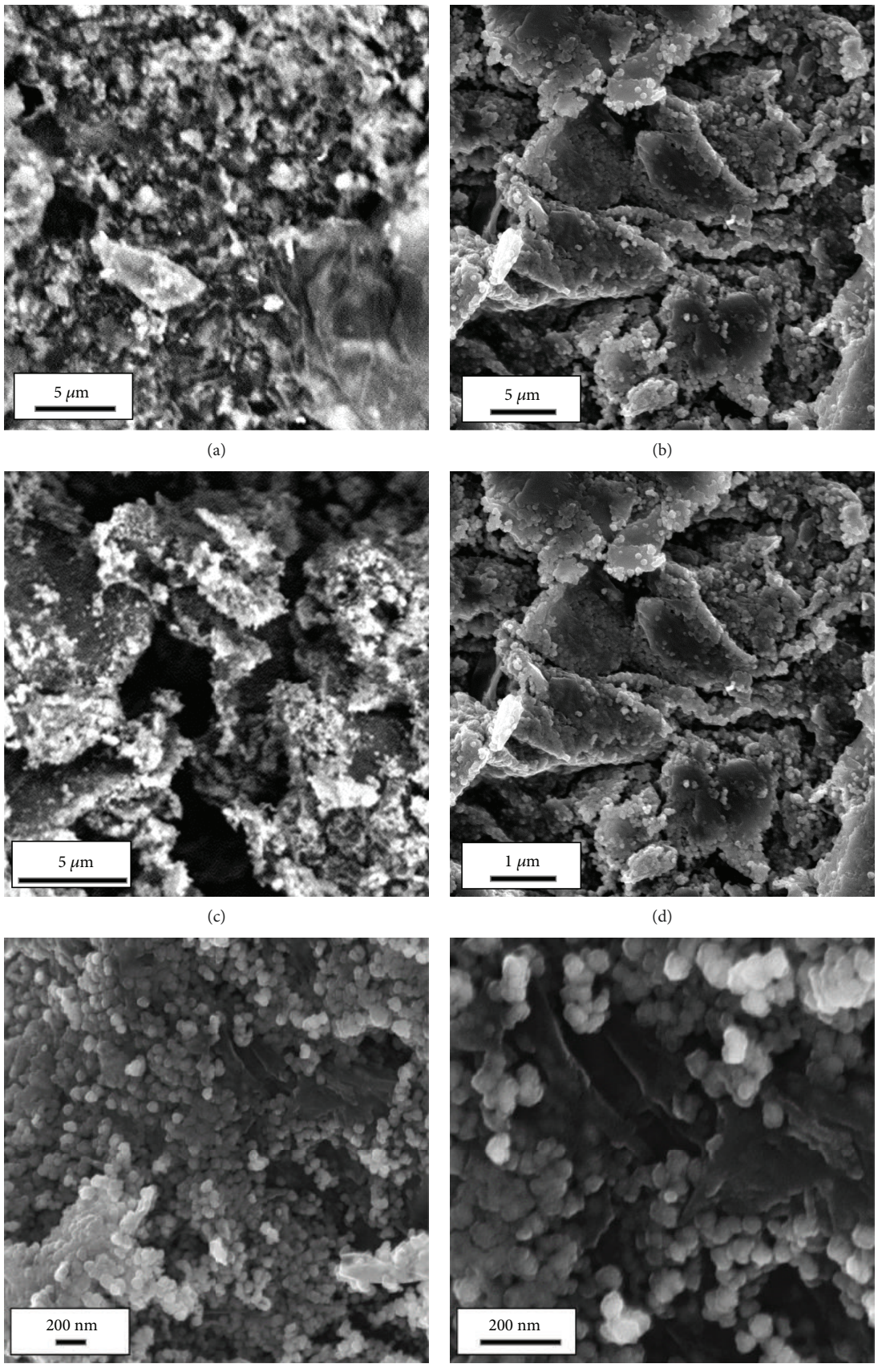

Figure 1: SEM images of (a) CoO@rGO, (b) $CoFe_2O_4$@rGO, and (c–f) Fe_2O_3@rGO nanocomposites.

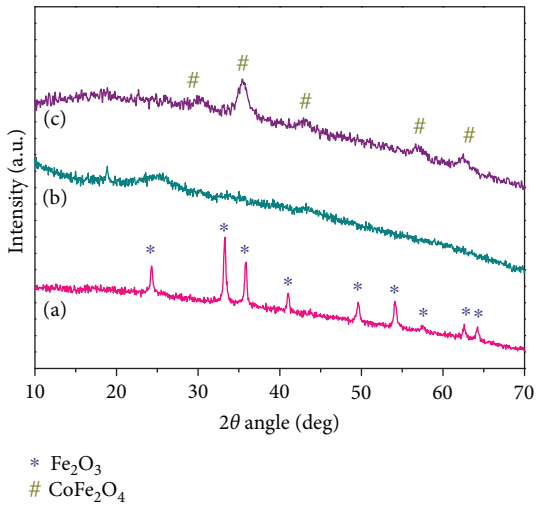

FIGURE 2: XRD patterns of (a) Fe_2O_3@rGO, (b) CoO@rGO, and (c) $CoFe_2O_4$@ rGO nanocomposites.

observed, proving the successful reduction of GO to rGO during the solvothermal treatment also in the presence of the salt precursor(s). However, due to their low intensity with respect to the diffraction peaks arising from the oxide, no signal from rGO is generally detected. Only in Figure 2(b), the broad peak corresponding to the reflection from (002) graphitic plane is visible at ~25° 2θ angle.

As for the crystalline phase of the TMOs, the formation of hematite is observed when $Fe(CH_3COO)_2$ alone is used as a precursor (Figure 2(a)). In fact, the diffraction peaks at 24.1°, 33.2°, 35.8°, 40.9°, 49.5°, 53.9°, 57. 5°, 62.6°, and 64.1° 2θ angles can be indexed to the (012), (104), (110), (113), (024), (116), (122), (214), and (300) crystal planes of the rhombohedral (hexagonal) structure of hematite (JCPDS card no. 33-0664), respectively [37]. The average size of α-Fe_2O_3 crystallites, evaluated from the main (104) peak of the diffractogram via the Scherrer equation, is 27.2 nm (i.e., smaller than the average grain size estimated from the higher-magnification SEM images), proving the polycrystalline nature of the oxide NPs.

When $Co(CH_3COO)_2{\cdot}4H_2O$ alone is utilized, no evident diffraction peaks are detected in the XRD pattern of the nanocomposite, probably due to the amorphous nature of the oxide formed (Figure 2(b)). Conversely, when both $Fe(CH_3COO)_2$ and $Co(CH_3COO)_2{\cdot}4H_2O$ are used, broad and less sharp reflection peaks at 30.1°, 35.4°, 43.1°, 56.9°, and 62.5° 2θ angles are observed (Figure 2(c)), which, respectively, correspond to the (220), (311), (400), (511), and (440) crystal planes of the cubic spinel structure of cobalt ferrite ($CoFe_2O_4$, JCPDS card no. 22-1086) [38]. The results of EDX analysis (Figure S6) confirm the formation of $CoFe_2O_4$@rGO: the Fe/Co atomic ratio (~2 : 1) is found to be very close to the stoichiometric ratio of $CoFe_2O_4$.

Figure 3 displays micro-Raman spectra of the investigated nanocomposites. Hematite belongs to the trigonal D_3d_6 space group symmetry. Normal modes predicted by the factor group analysis include six IR-active vibrations ($2A_{2u} + 4E_u$) and seven Raman-active vibrations ($2A_{1g} + 5E_g$) [39–41]. Actually, six peaks at 224, 244, 293, 407, 496, and 609 cm^{-1} are detected in the Raman spectrum of bare hematite (Figure 3(a)), corresponding to the $A_{1g}(1)$, $E_g(1)$, unresolved $E_g(2)$-$E_g(3)$, $E_g(4)$, $A_{1g}(2)$, and $E_g(5)$ vibration modes, respectively. In addition, a very weak band near 660 cm^{-1} is observed, due to the presence of surface defects and/or reduced grain size which, relaxing selection rules, render Raman active the IR-active E_u mode [39]. The very intense asymmetric band peaking at ~1315 cm^{-1} is ascribed to two-phonon scattering or two-magnon scattering [42].

The spectra of TMO@rGO nanocomposites (Figures 3(b)–3(d)) are dominated by the D- and G-bands arising from the Csp^2 modes of rGO support. In agreement with XRD analysis results, no additional modes are detected in the nanocomposite synthesized by using $Co(CH_3COO)_2{\cdot}4H_2O$ as a precursor (Figure 3(c)), while the modes of hematite (with the most intense band overlapped to the D-band) are visible in Fe_2O_3@rGO nanocomposite (Figure 3(b)).

Cobalt ferrite with a cubic structure belongs to the space group Fd3m [43, 44]. For the spinel structure, factor group analysis predicts five Raman active phonon modes ($A_{1g} + E_g + 3T_{2g}$). In the spectrum of the $CoFe_2O_4$@rGO composite (Figure 3(d)), only three spectral features are visible at ~285, 471, and 683 cm^{-1}, which can be ascribed to the Raman vibration modes of ferrimagnetic $CoFe_2O_4$.

Figures 4 and 5 show the high-resolution photoelectron spectra of the Fe 2p and Co 2p core levels in nanocomposites synthesized by the use of $Fe(CH_3COO)_2$ and/or of $Co(CH_3COO)_2{\cdot}4H_2O$ precursor(s). In the Fe 2p spectra (Figure 4), the binding energy (BE) position and separation of $2p_{3/2}$ (710.4 eV) and $2p_{1/2}$ (724.0 eV) spin-orbit components and the presence of the corresponding shake-up satellites at 718.9 eV and 733.0 eV indicate that the dominant state of Fe ions is +3 [45]. For the $CoFe_2O_4$@rGO composite (Figure 4(b)), the broad band at 710.4 eV may indicate also the presence of some Fe^{2+} [46]. In the Co 2p spectra (Figures 5), the BE positions of the two spin-orbit components ($2p_{3/2}$ at 780.6 eV and $2p_{1/2}$ at 798.0 eV) with the related shake-up satellites, respectively, at 786.6 eV and 803 eV are indicative of Co ions in the +2 state [47].

The asymmetry featuring the spectral profile of the Co 2p core level photoelectron spectrum in $CoFe_2O_4$@rGO nanocomposite (Figures 5(b)) is indicative of the presence of two nonequivalent bonds of Co ions, typical of $CoFe_2O_4$ compounds [47].

The indications emerging from XPS analysis allow understanding the lack of oxide-related contributions in the Raman spectrum of CoO@rGO nanocomposite (Figure 3(c)). Cobalt oxide exists in two stable forms, Co_3O_4 and CoO. In Co(II) oxide, characterized by a face-centered cubic crystalline structure, the first-order phonon Raman scattering is forbidden, while the (allowed) second-order is visible in the 1000–1100 cm^{-1} spectral range as a large band with weak intensity [48]. The very intense D- and G-bands hinder its detection in the spectrum of CoO@rGO nanocomposite.

Additional information is inferred from the high-resolution photoelectron spectra of the O 1s core level

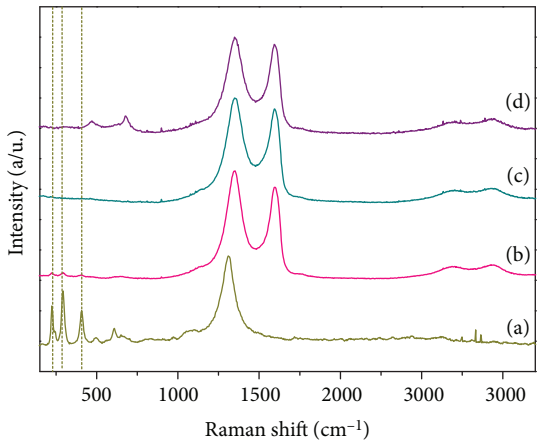

Figure 3: Micro-Raman spectra of (a) bare Fe_2O_3, (b) Fe_2O_3@rGO, (c) CoO@rGO, and (d) $CoFe_2O_4$@rGO nanocomposites.

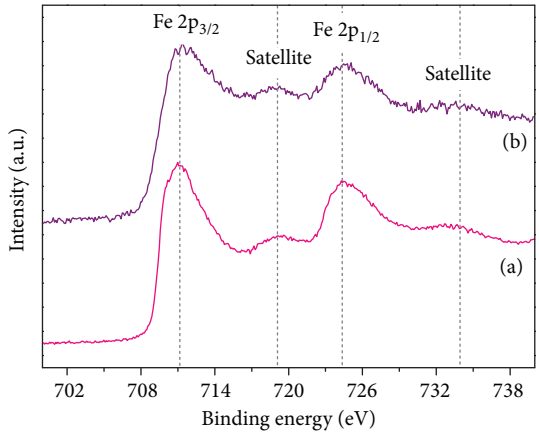

Figure 4: High-resolution photoelectron spectra of the Fe 2p core levels in (a) Fe_2O_3@rGO and (b) $CoFe_2O_4$@rGO nanocomposites.

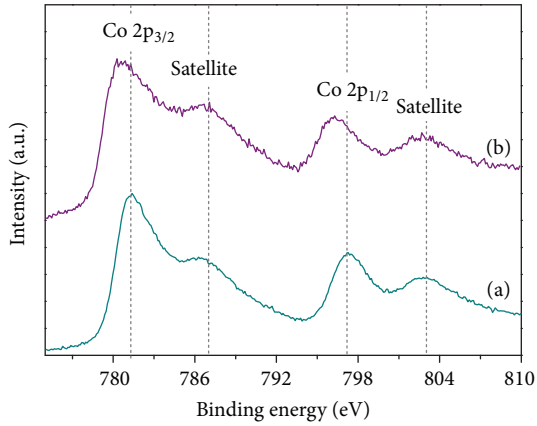

Figure 5: High-resolution photoelectron spectra of the Co 2p core levels in (a) CoO@rGO and (b) $CoFe_2O_4$@rGO nanocomposites.

(Figure S7). Fe_2O_3@rGO and $CoFe_2O_4$@rGO nanocomposites exhibit similar spectral profiles (a and c in Figure S7). The most intense contribution, centered at about 530 eV in both the spectra, corresponds to the O^{2-} typical of Fe_2O_3 lattice and is compatible with O^{2-} anions in the $CoFe_2O_4$ coordination [49]. On the contrary, in CoO@rGO nanocomposite, the O 1s profile (b in Figure S7) is dominated by the contribution due to C=O species in carbonyl and/or carboxylic groups at 532.3 eV [50]. Indeed, in the high-resolution photoelectron spectra of the C 1s core level of CoO@rGO nanocomposite (b in Figure S8), a strong contribution ascribable to carboxylic groups is detected, and the highest O/C atomic ratio (Table S1) pertains to this composite. On the contrary, in Fe_2O_3@rGO and $CoFe_2O_4$@rGO nanocomposites, the carbonaceous support exhibits a higher reduction degree (i.e., lower O/C atomic ratio), as evident from the C 1s photoelectron spectra (a and c in Figure S8).

The relative weight of the transition metal oxide (rGO) in the investigated nanocomposites, as estimated on the basis of the XPS compositional analysis (Table S1), is 55.1, 59.3, and 74.1 wt% (44.9, 40.7, and 25.9 wt%) for CoO@rGO, Fe_2O_3@rGO, and $CoFe_2O_4$@rGO, respectively.

3.3. Electrochemical Behavior. The results of rate capability tests on bare Fe_2O_3, Fe_2O_3@rGO nanocomposite, and Fe_2O_3+rGO physical mixture are presented in Figure 6. The comparison between their specific capacities demonstrates the beneficial effect of the rGO support, in agreement with the results of other studies [29, 31]. Fe_2O_3@rGO nanocomposite exhibits a higher specific capacity compared with the bare hematite. Indeed, a first anodic specific capacity of 331.4 mAh/g is registered for the composite, while only 129.2 mAh/g is obtained for bare Fe_2O_3. However, the high initial specific capacity of the Fe_2O_3@rGO is not fully reversible, and after 10 cycles at a C/20 rate, the anodic specific capacity becomes 181.4 mAh/g. Nonetheless, in the subsequent cycles, the capacity retention increases, and in the last 10 cycles at a C/20 rate, a highly stable specific capacity of 166.0 mAh/g (40% higher than that for bare Fe_2O_3) is recovered.

The comparison between specific capacities of Fe_2O_3@rGO nanocomposite and Fe_2O_3+rGO physical mixture demonstrates the importance of an intimate connection between the carbonaceous support and the oxide anchored on its surface. As a matter of fact, in the first cycles, the specific capacities of Fe_2O_3@rGO and Fe_2O_3+rGO are comparable, but at higher rates, the difference becomes more evident. At C/2 and 2C rates, the nanocomposite outperforms the physical mixture. This is particularly evident at the highest rate. At 2C, in Fe_2O_3+rGO, the specific capacity decreases down to 20 mAh/g, whereas Fe_2O_3@rGO can still deliver 65 mAh/g. Moreover, when the current is set back to C/20, a better stability of the nanocomposite is registered, which proves its greater ability to buffer the volume changes occurring during the sodiation/desodiation process (i.e., a superior structural stability) with respect to the physical mixture. Although a long-term cycling analysis is still needed, these preliminary results clearly prove that the *intimate* contact between iron oxide and conductive rGO support, peculiar to the nanocomposite, leads to improved structural stability and, hence, to better rate performance.

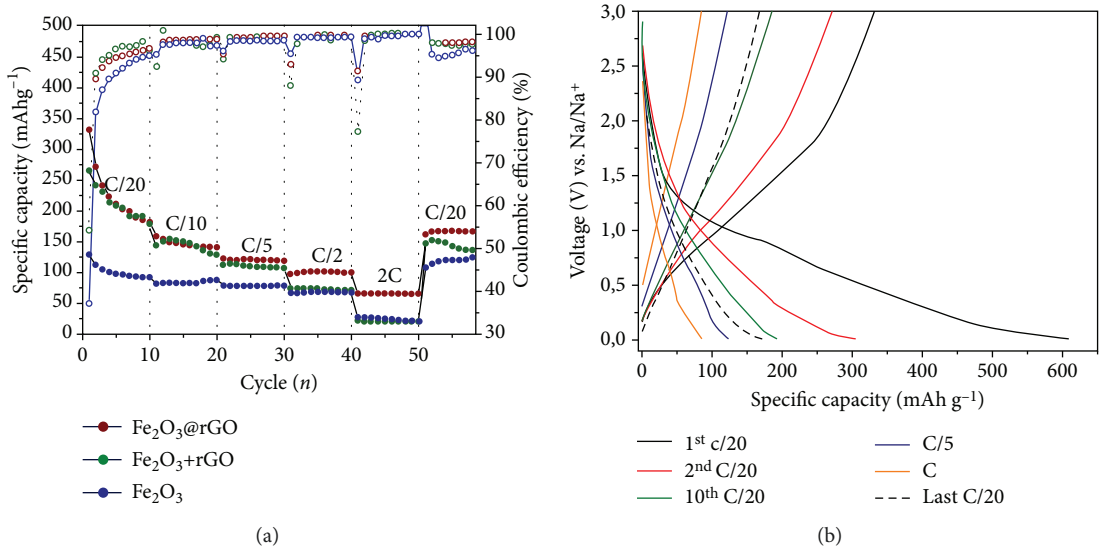

Figure 6: (a) Anodic specific capacity and columbic efficiency as a function of the number of cycles, as obtained from the GCPL for electrodes based on bare Fe_2O_3, Fe_2O_3@rGO nanocomposite, and Fe_2O_3+rGO physical mixture. (b) Voltage versus specific capacity for selected cycles of the Fe_2O_3@rGO nanocomposite.

The low columbic efficiency (CE) that all active materials exhibit in the first cycle is generally attributed to the decomposition of the electrolyte and the formation of the solid electrolyte interface (SEI) [51]. Indeed, by analyzing the first charge/discharge profiles of Fe_2O_3@rGO (CE = 54.3%) presented in Figure 6(b), the process centered at 1.0 V, generally attributed to the SEI formation, appears only during the first sodiation [52].

In the next cycles, CE rapidly increases reaching values higher than 99%. Finally, after the first cycle, during the sodiation, a two-step process takes place, which could be assigned to the insertion of sodium in the oxide and the conversion of iron [22, 53]. The results here reported are comparable with what were reported in literature, but the relative low temperature (170°C) and the easy scalability of the one-step hydrothermal synthesis can be surpassingly advantageous.

As known from the literature [27, 29, 54], the solvothermal method allows obtaining a uniform and quasi-quantitative distribution of TMO on graphene. Moreover, the TMO to rGO mass ratio, which, as shown by Zhang et al. [29] and by Liu et al. [31], affects the electrochemical performance of the TMO@rGO nanocomposite, can be easily tuned. Finding the optimal TMO to rGO mass ratio for the investigated nanocomposites is out of the aims of the present work, and it might be the subject of a future study. Fe_2O_3@rGO nanocomposite with optimized Fe_2O_3 to rGO mass ratio might exhibit improved electrochemical performance with respect to that here presented.

4. Conclusions

In conclusion, transition metal oxides on reduced graphene oxide (TMO@rGO) nanocomposites, consisting of TMO nanoparticles uniformly anchored onto the surface of graphene nanosheets, were successfully synthesized via the one-step solvothermal process and characterized by means of a combination of complementary techniques. Fe_2O_3@rGO, $CoFe_2O_4$@rGO, and CoO@rGO were obtained by using Fe and/or Co acetates as oxide precursors.

The results of preliminary tests aimed at evaluating the electrochemical performance of Fe_2O_3@rGO as anode material for sodium ion rechargeable batteries demonstrate that the intimate contact between the carbonaceous support and the oxide anchored on its surface plays a crucial role. Fe_2O_3@rGO nanocomposite exhibits better rate capability and stability with respect to both bare Fe_2O_3 and Fe_2O_3+rGO physical mixture, as it is able to buffer the volume changes occurring during the sodiation/desodiation process.

Data Availability

The data (SEM, XRD, micro-Raman, and XPS (Fe 2p and Co 2p) relative to composites) used to support the findings of this study are included within the article.

Conflicts of Interest

The authors declare that there is no conflict of interest regarding the publication of this paper.

Supplementary Materials

Supplementary Materials include a schematic representation of the solvothermal treatment leading to the formation of the TMO@rGO nanocomposites; the elemental composition of the nanocomposites estimated from quantitative analysis of the XPS spectra; results of XRD, MRS, XPS, and SEM analyses on GO and rGO; EDX spectrum of CoFe2O4@rGO nanocomposite; and photoelectron spectra of the O 1s and C 1s core levels in the nanocomposites. *(Supplementary Materials)*

References

[1] F. Li, X. Jiang, J. Zhao, and S. Zhang, "Graphene oxide: a promising nanomaterial for energy and environmental applications," *Nano Energy*, vol. 16, pp. 488–515, 2015.

[2] L.-L. Tan, S.-P. Chai, and A. R. Mohamed, "Synthesis and applications of graphene-based TiO_2 photocatalysts," *ChemSusChem*, vol. 5, no. 10, pp. 1868–1882, 2012.

[3] Q. Li, N. Mahmood, J. Zhu, Y. Hou, and S. Sun, "Graphene and its composites with nanoparticles for electrochemical energy applications," *Nano Today*, vol. 9, no. 5, pp. 668–683, 2014.

[4] K. T. Nguyen and Y. Zhao, "Integrated graphene/nanoparticle hybrids for biological and electronic applications," *Nanoscale*, vol. 6, no. 12, pp. 6245–6266, 2014.

[5] V. Singh, D. Joung, L. Zhai, S. Das, S. I. Khondaker, and S. Seal, "Graphene based materials: past, present and future," *Progress in Materials Science*, vol. 56, no. 8, pp. 1178–1271, 2011.

[6] B. F. Machado and P. Serp, "Graphene-based materials for catalysis," *Catalysis Science & Technology*, vol. 2, no. 1, pp. 54–75, 2012.

[7] H.-J. Choi, S.-M. Jung, J.-M. Seo, D. W. Chang, L. Dai, and J. B. Baek, "Graphene for energy conversion and storage in fuel cells and supercapacitors," *Nano Energy*, vol. 1, no. 4, pp. 534–551, 2012.

[8] O. C. Compton and S. T. Nguyen, "Graphene oxide, highly reduced graphene oxide, and graphene: versatile building blocks for carbon-based materials," *Small*, vol. 6, no. 6, pp. 711–723, 2010.

[9] Z.-S. Wu, G. Zhou, L.-C. Yin, W. Ren, F. Li, and H. M. Cheng, "Graphene/metal oxide composite electrode materials for energy storage," *Nano Energy*, vol. 1, no. 1, pp. 107–131, 2012.

[10] A. W. Anwar, A. Majeed, N. Iqbal et al., "Specific capacitance and cyclic stability of graphene based metal/metal oxide nanocomposites: a review," *Journal of Materials Science & Technology*, vol. 31, no. 7, pp. 699–707, 2015.

[11] S. Park and R. S. Ruoff, "Chemical methods for the production of graphenes," *Nature Nanotechnology*, vol. 4, no. 4, pp. 217–224, 2009.

[12] Y. Zhu, S. Murali, W. Cai et al., "Graphene and graphene oxide: synthesis, properties, and applications," *Advanced Materials*, vol. 22, no. 35, pp. 3906–3924, 2010.

[13] H.-L. Guo, X. F. Wang, Q. Y. Qian, F. B. Wang, and X. H. Xia, "A green approach to the synthesis of graphene nanosheets," *ACS Nano*, vol. 3, no. 9, pp. 2653–2659, 2009.

[14] L. Chen, H. Yu, J. Zhong, J. Wu, and W. Su, "Graphene based hybrid/composite for electron field emission: a review," *Journal of Alloys and Compounds*, vol. 749, pp. 60–84, 2018.

[15] M. Fathy, A. Gomaa, F. A. Taher, M. M. El-Fass, and A. E. H. B. Kashyout, "Optimizing the preparation parameters of GO and rGO for large-scale production," *Journal of Materials Science*, vol. 51, no. 12, pp. 5664–5675, 2016.

[16] Z. Xing, J. Tian, A. M. Asiri, A. H. Qusti, A. O. Al-Youbi, and X. Sun, "Two-dimensional hybrid mesoporous Fe_2O_3–graphene nanostructures: a highly active and reusable peroxidase mimetic toward rapid, highly sensitive optical detection of glucose," *Biosensors and Bioelectronics*, vol. 52, pp. 452–457, 2014.

[17] L. Wang, Z. Wei, M. Mao, H. Wang, Y. Li, and J. Ma, "Metal oxide/graphene composite anode materials for sodium-ion batteries," *Energy Storage Materials*, vol. 16, pp. 434–454, 2019.

[18] M. V. Reddy, G. V. Subba Rao, and B. V. R. Chowdari, "Metal oxides and oxysalts as anode materials for Li ion batteries," *Chemical Reviews*, vol. 113, no. 7, pp. 5364–5457, 2013.

[19] Y. Wang, C. Wu, Z. Wu et al., "FeP nanorod arrays on carbon cloth: a high-performance anode for sodium-ion batteries," *Chemical Communications*, vol. 54, no. 67, pp. 9341–9344, 2018.

[20] K. Cao, T. Jin, L. Yang, and L. Jiao, "Recent progress in conversion reaction metal oxide anodes for Li-ion batteries," *Materials Chemistry Frontiers*, vol. 1, no. 11, pp. 2213–2242, 2017.

[21] S. Santangelo, M. Fiore, F. Pantò et al., "Electro-spun Co_3O_4 anode material for Na-ion rechargeable batteries," *Solid State Ionics*, vol. 309, pp. 41–47, 2017.

[22] M. Fiore, G. Longoni, S. Santangelo et al., "Electrochemical characterization of highly abundant, low cost iron (III) oxide as anode material for sodium-ion rechargeable batteries," *Electrochimica Acta*, vol. 269, pp. 367–377, 2018.

[23] Y. Jiang, M. Hu, D. Zhang et al., "Transition metal oxides for high performance sodium ion battery anodes," *Nano Energy*, vol. 5, pp. 60–66, 2014.

[24] X. Ji, S. Hao, F. Qu et al., "Core–shell $CoFe_2O_4$@Co–Fe–Bi nanoarray: a surface-amorphization water oxidation catalyst operating at near-neutral pH," *Nanoscale*, vol. 9, no. 23, pp. 7714–7718, 2017.

[25] H.-W. Wang, Z.-A. Hu, Y.-Q. Chang et al., "Facile solvothermal synthesis of a graphene nanosheet–bismuth oxide composite and its electrochemical characteristics," *Electrochimica Acta*, vol. 55, no. 28, pp. 8974–8980, 2010.

[26] S. Huang, Y. Jin, and M. Jia, "Preparation of graphene/Co_3O_4 composites by hydrothermal method and their electrochemical properties," *Electrochimica Acta*, vol. 95, pp. 139–145, 2013.

[27] J. Zhu, T. Zhu, X. Zhou et al., "Facile synthesis of metal oxide/reduced graphene oxide hybrids with high lithium storage capacity and stable cyclability," *Nanoscale*, vol. 3, no. 3, pp. 1084–1089, 2011.

[28] B. S. Singu and K. R. Yoon, "Exfoliated graphene-manganese oxide nanocomposite electrode materials for supercapacitor," *Journal of Alloys and Compounds*, vol. 770, pp. 1189–1199, 2019.

[29] Z.-J. Zhang, Y.-X. Wang, S.-L. Chou, H. J. Li, H. K. Liu, and J. Z. Wang, "Rapid synthesis of α-Fe_2O_3/rGO nanocomposites by microwave autoclave as superior anodes for sodium-ion batteries," *Journal of Power Sources*, vol. 280, pp. 107–113, 2015.

[30] Z. Qiang, Y. M. Chen, B. Gurkan et al., "Cooperatively assembled, nitrogen-doped, ordered mesoporous carbon/iron oxide nanocomposites for low-cost, long cycle life sodium-ion batteries," *Carbon*, vol. 116, pp. 286–293, 2017.

[31] X. Liu, T. Chen, H. Chu et al., "Fe_2O_3-reduced graphene oxide composites synthesized via microwave-assisted method for sodium ion batteries," *Electrochimica Acta*, vol. 166, pp. 12–16, 2015.

[32] W. S. Hummers Jr. and R. E. Offeman, "Preparation of graphitic oxide," *Journal of the American Chemical Society*, vol. 80, no. 6, p. 1339, 1958.

[33] H.-W. Wang, Z.-A. Hu, Y.-Q. Chang et al., "Preparation of reduced graphene oxide/cobalt oxide composites and their enhanced capacitive behaviors by homogeneous incorporation of reduced graphene oxide sheets in cobalt oxide matrix,"

Materials Chemistry and Physics, vol. 130, no. 1-2, pp. 672–679, 2011.

[34] Y.-X. Wang, S.-L. Chou, H.-K. Liu, and S. X. Dou, "Reduced graphene oxide with superior cycling stability and rate capability for sodium storage," *Carbon*, vol. 57, pp. 202–208, 2013.

[35] A. C. Ferrari and J. Robertson, "Interpretation of Raman spectra of disordered and amorphous carbon," *Physical Review B*, vol. 61, no. 20, pp. 14095–14107, 2000.

[36] S. Santangelo, "Controlled surface functionalization of carbon nanotubes by nitric acid vapors generated from subazeotropic solution," *Surface and Interface Analysis*, vol. 48, no. 1, pp. 17–25, 2016.

[37] G. Wang, T. Liu, Y. Luo et al., "Preparation of Fe_2O_3/graphene composite and its electrochemical performance as an anode material for lithium ion batteries," *Journal of Alloys and Compounds*, vol. 509, no. 24, pp. L216–L220, 2011.

[38] H. Yang, K. Zhang, Y. Wang, C. Yan, and S. Lin, "$CoFe_2O_4$ derived-from bi-metal organic frameworks wrapped with graphene nanosheets as advanced anode for high-performance lithium ion batteries," *Journal of Physics and Chemistry of Solids*, vol. 115, pp. 317–321, 2018.

[39] A. Zoppi, C. Lofrumento, E. M. Castellucci, and P. Sciau, "Al-for-Fe substitution in hematite: the effect of low Al concentrations in the Raman spectrum of Fe_2O_3," *Journal of Raman Specroscopy*, vol. 39, no. 1, pp. 40–46, 2008.

[40] I. V. Chernyshova, M. F. Hochella Jr., and A. S. Madden, "Size-dependent structural transformations of hematite nanoparticles. 1. Phase transition," *Physical Chemistry Chemical Physics*, vol. 9, no. 14, pp. 1736–1750, 2007.

[41] S. Chaudhari and M. Srinivasan, "1D hollow α-Fe_2O_3 electrospun nanofibers as high performance anode material for lithium ion batteries," *Journal of Materials Chemistry*, vol. 22, no. 43, pp. 23049–23056, 2012.

[42] D. Bersani, P. P. Lottici, and A. Montenero, "Micro-Raman investigation of iron oxide films and powders produced by sol–gel syntheses," *Journal of Raman Specroscopy*, vol. 30, no. 5, pp. 355–360, 1999.

[43] P. Chandramohan, M. P. Srinivasan, S. Velmurugan, and S. V. Narasimhan, "Cation distribution and particle size effect on Raman spectrum of $CoFe_2O_4$," *Journal of Solid State Chemistry*, vol. 184, no. 1, pp. 89–96, 2011.

[44] B. J. Rani, M. Ravina, B. Saravanakumar et al., "Ferrimagnetism in cobalt ferrite ($CoFe_2O_4$) nanoparticles," *Nano-Structures & Nano-Objects*, vol. 14, pp. 84–91, 2018.

[45] J.-B. Moussy, "From epitaxial growth of ferrite thin films to spin-polarized tunnelling," *Journal of Physics D: Applied Physics*, vol. 46, no. 14, pp. 143001–143028, 2013.

[46] J. A. Moyer, C. A. F. Vaz, E. Negusse, D. A. Arena, and V. E. Henrich, "Controlling the electronic structure of $Co_{1-x}Fe_{2+x}O_4$ thin films through iron doping," *Physical Review B: Condensed Matter and Materials Physics*, vol. 83, no. 3, article 035121, 2011.

[47] Z. Zhou, Y. Zhang, Z. Wang et al., "Electronic structure studies of the spinel $CoFe_2O_4$ by X-ray photoelectron spectroscopy," *Applied Surface Science*, vol. 254, no. 21, pp. 6972–6975, 2008.

[48] Y. Li, W. Qiu, F. Qin et al., "Identification of cobalt oxides with Raman scattering and Fourier transform infrared spectroscopy," *Journal of Physical Chemistry C*, vol. 120, no. 8, pp. 4511–4516, 2016.

[49] S. Nappini, E. Magnano, F. Bondino et al., "Surface charge and coating of $CoFe_2O_4$ nanoparticles: evidence of preserved magnetic and electronic properties," *Journal of Physical Chemistry C*, vol. 119, no. 45, pp. 25529–25541, 2015.

[50] A. Cossaro, M. Puppin, D. Cvetko et al., "Tailoring SAM-on-SAM formation," *Journal of Physical Chemistry Letters*, vol. 2, no. 24, pp. 3124–3129, 2011.

[51] B. Nageswara Rao, P. Ramesh Kumar, O. Padmaraj, M. Venkateswarlu, and N. Satyanarayana, "Rapid microwave assisted hydrothermal synthesis of porous α-Fe_2O_3 nanostructures as stable and high capacity negative electrode for lithium and sodium ion batteries," *RSC Advances*, vol. 5, no. 44, pp. 34761–34768, 2015.

[52] B. Philippe, M. Valvo, F. Lindgren, H. Rensmo, and K. Edström, "Investigation of the electrode/electrolyte interface of Fe_2O_3 composite electrodes: Li vs Na batteries," *Chemistry of Materials*, vol. 26, no. 17, pp. 5028–5041, 2014.

[53] B. Huang, K. Tai, M. Zhang, Y. Xiao, and S. J. Dillon, "Comparative study of Li and Na electrochemical reactions with iron oxide nanowires," *Electrochimica Acta*, vol. 118, pp. 143–149, 2014.

[54] S. Y. Liu, J. Xie, Q. Pan et al., "Graphene anchored with nanocrystal Fe_2O_3 with improved electrochemical Li-storage properties," *International Journal of Electrochemical Science*, vol. 7, pp. 354–362, 2012.